Surface-plasmon-polariton hybridized cavity modes in submicrometer slits in a thin Au film

R. Walther,[1,2] S. Fritz,[1,*] E. Müller,[1] R. Schneider,[1] T. Maniv,[3] H. Cohen,[4] C. Matyssek,[5] K. Busch,[5,6] and D. Gerthsen[1,2]

[1]*Laboratorium für Elektronenmikroskopie, Karlsruher Institut für Technologie, D-76128 Karlsruhe, Germany*

[2]*Center for Functional Nanostructures, Karlsruhe Institute of Technology, D-76128 Karlsruhe, Germany*

[3]*Schulich Faculty of Chemistry, Technion-Israel Institute of Technology, Haifa 32000, Israel*

[4]*Department of Chemical Research Support, Weizmann Institute of Science, Rehovot 76100, Israel*

[5]*Humboldt-Universität zu Berlin, Institut für Physik, AG Theoretische Optik & Photonik, D-12489 Berlin, Germany*

[6]*Max-Born-Institut, 12489 Berlin, Germany*

(Received 9 February 2016; revised manuscript received 17 May 2016; published 17 June 2016)

The excitation of cavity standing waves in double-slit structures in thin gold films, with slit lengths between 400 and 2560 nm, was probed with a strongly focused electron beam in a transmission electron microscope. The energies and wavelengths of cavity modes up to the 11th mode order were measured with electron energy loss spectroscopy to derive the corresponding dispersion relation. For all orders, a significant redshift of mode energies accompanied by a wavelength elongation relative to the expected resonator energies and wavelengths is observed. The resultant dispersion relation is found to closely follow the well-known dispersion law of surface-plasmon polaritons (SPPs) propagating on a gold/air interface, thus providing direct evidence for the hybridized nature of the detected cavity modes with SPPs.

DOI: 10.1103/PhysRevB.93.245417

Electromagnetic waves interact strongly with metallic nanostructures by the excitation of plasmons and surface plasmons. Such waves coupled to surface plasmons at the surface, denoted as surface-plasmon polaritons (SPPs), play a dominant role in the miniaturization of nanophotonic devices [1,2] and are subject to numerous studies [3–5]. However, despite substantial recent progress of near-field optical techniques, investigations of such structures via light optical techniques are hampered by their limited spatial resolution [6]. Hence, electron microscopy combined with electron energy loss spectroscopy (EELS) has recently become an interesting tool for studying the optoelectronic properties of such nanostructures [7]. The application of electron microscopy in the field of plasmonics is based on the ability of swift electrons (i) to excite surface plasmons [8] and (ii) to image surface-plasmon resonances in confined systems with a spatial resolution on the nanometer scale. Meanwhile, numerous studies of the plasmonic properties of nanoscaled objects are available. For instance, localized surface-plasmon resonances of single nanoparticles were revealed by several groups [9–16]. Rossouw and Botton [17] studied the plasmonic response of silver nanowires and were able to resolve guided SPPs with energies as low as 0.17 eV. Another example is the analysis of the coupling between split ring resonators in metamaterials by von Cube *et al.* [18].

Specifically, following the discovery of the so-called enhanced transmission of light through subwavelength apertures (extraordinary optical transmission), the response of plasmonic nanostructures has raised enormous interest [19,20]. Both light-optical and electron-microscopy techniques are used to gain insight into the physical processes involved in this effect [20]. The optical response of circular and rectangular nanoscaled holes in a thin Ag film was studied by Sigle *et al.* [21] and Ögüt *et al.* [22]. In the latter work, Fabry-Perot-like surface-plasmon resonances along the length of rectangular single and double slits were detected. Based on the application of Babinet´s principle, it was shown that magnetic coupling between two closely spaced slits leads to hybridized surface-plasmon eigenmodes in a double-slit system. Carmeli *et al.* [23] studied microholes in an Au film by scanning transmission electron microscopy combined with EELS (STEM EELS) and were able to excite SPPs even when the electron beam was several 100 nm away from a metal wall. The scarcity of electron microscopy studies on nanoscale hole structures can be attributed to the low intensity and small energies of the corresponding signals, typically below 1 eV, that have to be retrieved from the EELS spectra. Walther *et al.* [24] studied how the introduction of a second slit influences the plasmonic response by STEM EELS and observed a significant enhancement of the hybridized SPP cavity mode due to coupling to the second slit. Simulations performed in real space and real time domain illustrated the mechanism of interslit coupling. SPPs, induced by the cavity modes, propagate at the upper and lower surfaces of the film, thus partly exciting similar SPP cavity modes in the second slit and partly being scattered into backpropagating SPPs. Coherent interference of the originally excited and backpropagating SPPs from the neighboring slit across the varying slit distance is responsible for the resulting mode intensities.

In this paper, STEM EELS was used to investigate the excitation of SPPs and associated cavity standing waves in submicrometer rectangular holes in a thin Au film. Using STEM EELS in a monochromated electron microscope is essential to detect weak low-energy SPP signals. Signals with energies as low as 0.24 eV could be retrieved—corresponding to the fundamental mode of cavity standing waves excited in the slits. This ability to extract low-energy signals from EELS spectra is the prerequisite in this paper for investigating: double-slit systems in a large range of slit lengths between 400 and 2560 nm. In addition to the energies, in all double-slit systems, the wavelengths of fundamental and higher-order cavity modes were measured. Taking advantage of the large

*Corresponding author: stefan.fritz@kit.edu

intensity enhancement under coupling to a neighboring slit, higher harmonics of the fundamental cavity mode up to the 11th order were observed, allowing for accurate determination of the dispersion relation and a direct test of the expected SPPs dispersion.

I. EXPERIMENTAL TECHNIQUES AND SIMULATION METHODS

A thin Au film was prepared by evaporating 200 nm Au onto a NaCl single-crystal substrate. The film was subsequently floated off and placed on a standard Au TEM grid. Double slits with a width of 180 nm and different lengths L of 400, 535, 645, 960, 1300, 1620, 1900, 2180, 2340, and 2560 nm were milled in the Au film using an FEI Strata 400S focused-ion-beam system. The metal bar between the slits has a width of 100 nm. Prior to the STEM EELS experiments, the specimens were plasma-cleaned for at least 3 min to remove organic residues from preparation. The experiments were performed in an FEI Titan³ 80-300 equipped with an electron monochromator (Wien filter type) and a Gatan imaging filter (GIF) Tridiem model 865 HR. Under monochromated conditions, a probe size of about 1 nm is realized. For short exposure times of 1 ms, the energy resolution is 0.11 eV, which is given by the full width at half maximum (FWHM) of the zero-loss peak (ZLP). Spectra with high signal-to-noise ratio were acquired by employing binned gain averaging [25]. Fifty spectra taken with an acquisition time of 1 ms were summed up after energy drift correction and normalized with respect to the height of the ZLP prior to further processing. The Richardson-Lucy (RL) algorithm [26,27] adapted to EELS [28,29] was applied to the data to recover weak signals hidden in the tail of the ZLP. The RL algorithm was implemented in a self-written script in DigitalMicrograph (Gatan) according to Al-Bakkar *et al.* [30]. The application of the algorithm sharpens the spectral features in EEL spectra by deconvolution with the point spread function of the employed detector system. A vacuum reference spectrum, taken without the specimen, is used as point spread function. The achievable energy resolution for our experimental setup is 70 meV. A biexponential fit is used to remove the background in EELS spectra. Two exponents are required to model the steep slope of the ZLP shoulder and the comparably shallow slope of the ZLP tail.

Numerical simulations were carried out using the discontinuous Galerkin time domain (DGTD) method [18,31,32] with the extensions that are necessary to perform EELS simulations. The only difference is that we used a pure scattered field formalism here, which gives direct access to the field induced by the electron. The permittivity of the gold film is approximated by a single Drude and three Lorentz terms, which gives a reasonable approximation to the data measured by Johnson and Christy [33] over the entire energy range. The gold film was simulated with a finite size of at least $3\times3\ \mu\text{m}^2$ to reduce artifacts from the edges. Except for a small feature around 0.4 eV, the spectrum is entirely free of artifacts. For slits with lengths $L < 1\ \mu$m, this is well below the fundamental resonance and hence no longer slits were simulated. The film was surrounded by air and perfectly matched layers in order to reduce reflections from the boundary of the computational domain. Third-order elements were used with element sizes down to 10 nm to accurately resolve the incident field of the electron. The simulated spectra were convoluted with a Gaussian function of 100 meV FWHM, accounting for the finite experimental energy resolution and the corresponding spectral broadening.

II. RESULTS AND DISCUSSION

Figure 1(a) shows the color-coded EELS intensity that was obtained from line scans acquired parallel to the outer slit wall [upper part of Fig. 1(a)] and close to the metal bar [lower part of Fig. 1(a)] in a double-slit system with a slit length $L = 960$ nm. The double-slit system is shown in the high-angle annular dark-field (HAADF) STEM image in the inset in Fig. 1(a). The color-coded intensity of the EELS spectra is presented as a function of position along the long slit wall and reveals Fabry-Perot-like cavity standing waves. The first four harmonics of a hybridized SPP cavity mode in addition to the surface plasmon of gold are observed. The energies of the four harmonics are 0.53, 1.1, 1.65, and 2.1 eV at the outer wall. A significant redshift is observed close to the inner wall, resulting in energies of 0.5, 1.02, 1.53, and 2.0 eV. The surface plasmon appears at 2.4 eV at both walls. The intensity of the modes is strongly enhanced near the inner wall. The same intensity scale is used for the upper and lower sections of Fig. 1(a) to clearly visualize the intensity enhancement

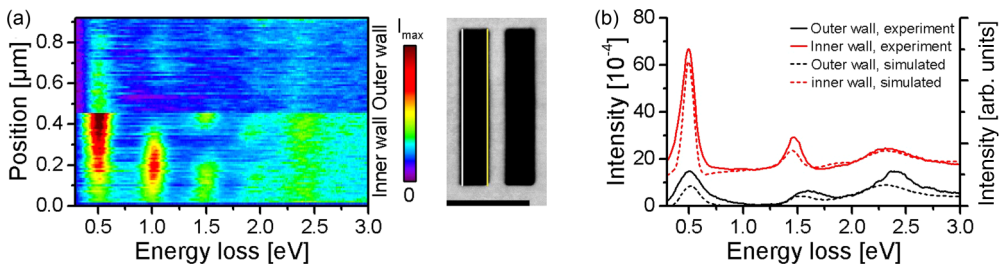

FIG. 1. (a) Color-coded EELS intensity obtained from line scans along the long slit wall in a double-slit system with slit length $L = 960$ nm. Intensity scans were performed at 10 nm distance to the outer wall (upper part of the graph) and to the inner wall (lower part of the graph). The intensity scale is identical in both cases. The inset shows an HAADF image of the double-slit system with a scale bar corresponding to 500 nm. The white line indicates the scan position at the outer and the yellow line at the inner wall. (b) Experimental (solid lines) and simulated (dashed lines) spectra acquired at $L/2$ and 10 nm distance to the outer wall (black lines) and the inner wall (red lines). Enhanced intensities and redshifts are observed for up to the third harmonic near the inner wall.

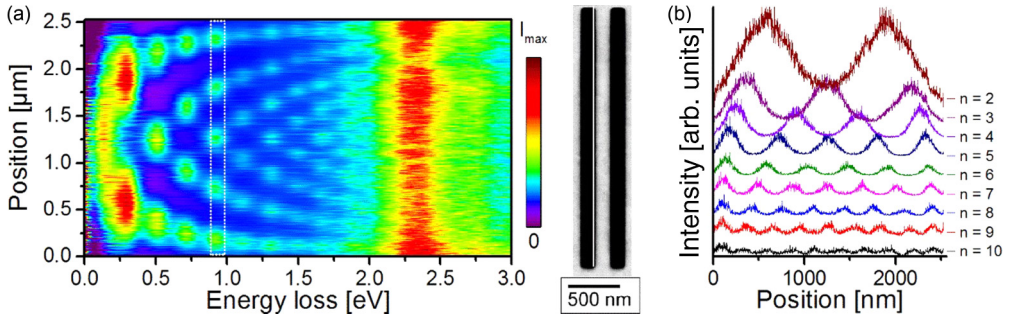

FIG. 2. (a) Color-coded EELS intensity as a function of position along the long slit wall. The EELS line scan was taken at 20 nm distance from the central metal bar in a 2560-nm-long double-slit system (cf. white line in HAADF STEM image). The intensity shows a behavior similar to Fabry-Perot-like standing waves along the long side of the slit. Higher harmonics up to the 11th order are observed. (b) Intensity profiles of the higher harmonics used for wavelength determination of the SPP cavity modes. The profiles are extracted from the color-coded intensity map by using 100 meV energy windows, indicated by the white dashed line rectangle for the fifth harmonic in (a).

close to the central metal bar. Figure 1(b) shows experimental and simulated spectra at $L/2$ near the outer and inner walls for the double-slit structure from Fig. 1(a). The spectra are shifted vertically for clarity. The fundamental mode, the third harmonic, and the surface plasmon are observed in the spectra. The second and fourth harmonics are absent at $L/2$ because they present, by definition, an antinode at this position. The spectra highlight the redshift and intensity enhancement of the cavity modes close to the inner wall. Simulated spectra confirm the experimental behavior. We note that the energies at either wall are significantly redshifted compared to a perfect electromagnetic resonator of length $L = 960$ nm, given by $E_n = \hbar c n/2L$ ($\hbar$: Planck constant; c: vacuum speed of light), with the expected energy of the fundamental mode ($n = 1$) at 0.65 eV. This discrepancy stems from the fact that either wall of the slit supports a SPP mode, and these modes tend to hybridize in narrow slits.

Similar cavity modes were reported for single-slit and double-slit systems in a thin Ag film by Ögüt *et al.* [22]. They observed the second, third, and fourth harmonics of the cavity modes and reported energy shifts due to hybridization of the SPPs supported by the different slit walls. The following hybridization scheme was proposed to explain their experimental findings. The starting point of this scheme is a single wall in an infinitely wide slit, with an SPP energy similar to a resonator of identical length. Upon introduction of a second wall, i.e., the realization of single slit, both wall SPPs hybridize into a high-energy and a low-energy mode. Only the low-energy mode is observed in their experiments, as the other one is weak. The high-energy mode corresponds to SPPs on either slit wall oscillating in phase, which, in turn, leads to a weak electromagnetic field in the slit. For a double slit, the two possible states of each slit interact with each other giving rise to further hybridization. As a result, there are four possible modes for a double-slit system. However, only the two modes associated with hybridization of the strongly excited single slit mode are observed. The experiments of Carmeli *et al.* [23] that were performed in 4500×900 nm and 900×180 nm slits in a gold film, confirm the abovementioned hybridization scheme of a single slit. In the wide slit (corresponding a single wall), they observed the fundamental mode at 0.65 eV, whereas it is shifted towards 0.5 eV for the narrow slit.

The energy shifts observed in our experiments can be readily related to the hybridization scheme of Ögüt *et al.* [22]. The SPP modes observed at the outer wall in a double-slit system correspond to the strongly excited single-slit mode, as experiments in single slits (not shown here) show identical energies. The energy shifts between the outer and inner wall are related to the further hybridization due to the second slit. In summary, in a double-slit system, the two degenerate low-energy modes of the single slit are split into a new low-energy and a high-energy mode. However, only the former is observed in the experimental data of Fig. 1. The splitting into low-energy and high-energy modes in double-slit systems was reported by Walther *et al.* [24,34]. In their studies, the distance between two slits was varied and the antisymmetric, low-energy mode was found to dominate the spectrum for small distances. For larger interslit distances, the high-energy mode is dominant.

To further study hybridized SPP cavity modes, several double-slit structures with slit lengths between 400 and 2560 nm were investigated. Figure 2 presents the results for the double-slit system with the largest length of 2560 nm. To visualize the excitation of higher-order harmonics, a longitudinal line scan was performed at 20 nm distance to the central metal bar (white line in the HAADF STEM image inset in Fig. 2(a). The data were treated with 20 iterations of the RL-algorithm and subsequent background subtraction. The fundamental mode is barely recognizable, as its energy of 0.22 eV is hidden in the tail of the ZLP and therefore difficult to resolve. The next 11 harmonics are discernible with a hint of even the 12th harmonic. The strong signal at about 2.4 eV is the Au surface plasmon. Figure 2(b) shows extracted intensity profiles of the second to 10th harmonic from the line scan of Fig. 2(a). The individual profiles for a specific harmonic were extracted using a 100 meV wide energy window [exemplarily indicated for the fifth harmonic by the white dashed rectangle in Fig. 2(a)]. From these profiles, the wavelengths of the cavity modes can be determined because the distance between two antinodes corresponds to half of the wavelength. The profile of the fundamental mode is not included due to the aforementioned problems in resolving its energy.

Figure 3 summarizes the measured energies of the fundamental mode and higher harmonics for different slit lengths,

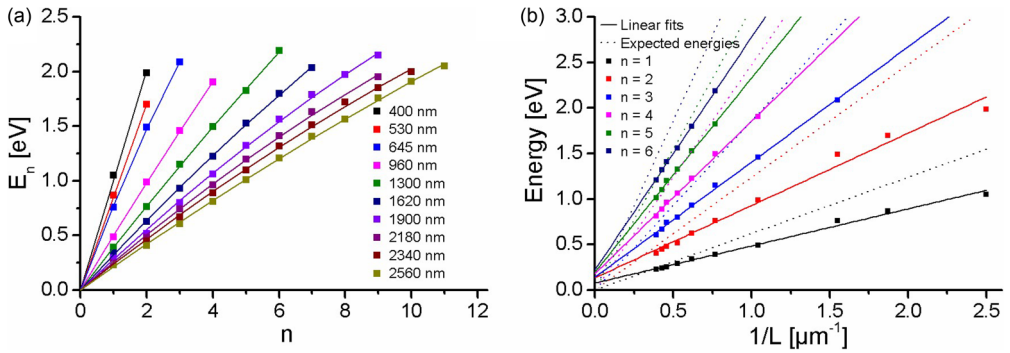

FIG. 3. (a) Energies of the fundamental mode and higher harmonics, ω_n, in double-slit systems with different lengths. The data were extracted from spectra acquired close to the thin metal bar between the two slits. The lines show second order polynomial least-square fits of the energy of the harmonics of the respective double slits, except for $L = 400$ nm and 535 nm, which were fitted by straight lines. (b) Measured energies of the first six harmonics plotted against the reciprocal slit length with linear least-square fits (solid lines) and the expected energies for a perfect resonator of the same length (dotted lines).

acquired at the inner wall. With increasing slit length from 400 to 2560 nm, a redshift of the fundamental mode from 1.0 to 0.22 eV is observed. A slight deviation from linearity is found in the energies of ω_n for increasing n. The lines in Fig. 3(a) are second order polynomial least-square fit curves of the energies of the fundamental and higher harmonics for a particular slit length, except for $L = 400$ and 535 nm, where a linear fit was applied. They are in good agreement with the experimental data and yield ω_1 values of 1.0 eV ($L = 400$ nm), 0.85 eV ($L = 535$ nm), 0.78 eV ($L = 645$ nm), 0.48 eV ($L = 960$ nm), 0.39 eV ($L = 1300$ nm), 0.32 eV ($L = 1620$ nm), 0.28 eV ($L = 1900$ nm), 0.26 eV ($L = 2180$ nm), 0.24 eV ($L = 2340$ nm), and 0.22 eV ($L = 2560$ nm). Measurements of such standing wavelike SPP modes on Au-Ag alloy nanowires were reported by Alber *et al.* [15]. They also observed slight deviations from a linear relation of the mode order n and its energy E_n. Figure 3(b) shows the measured energies of the first six harmonics at the inner wall, as a function of the reciprocal slit length, which can be well fitted by linear least-square fits (solid lines) in the form of $E(L) = m\,1/L + a$, with the slope m and the axis intercept a. An ideal resonator should have an axis intercept equal to zero. Its deviation from zero corresponds to a length correction of the slit. The introduction of an effective slit length and wavelength scaling was previously reported for nanorods by Novotny [35] and Schoen *et al.* [36]. Novotny [35] reported shorter effective slit lengths for nanorods—opposite of our findings for slits. However, this could be related to Babinet's principle that states complementary behavior for complementary structures [37]. Also included are the expected energies for ideal electromagnetic resonators of the same length (dashed lines) given by $E_n = hcn/2L$. The fit results are shown in Table I. The linear relationship between these two properties is expected and demonstrates that energy of the cavity standing waves can be well tuned in submicrometer slit cavities. The slope of the linear fit curves for the first six harmonics can be roughly related to each other by $m_n = n \cdot m_1$ with $m_1 = 0.41$ eVμm, similar to the energies which can be roughly calculated as $E_n = n \cdot E_1$. The slope of the fit curves for the experimental data is compared to the expected ideal slope m^* resulting from $E_n = hcn/2L$ given by 0.62 eV μm for $n = 1$, which is the expected slope for a single wall. The afore-mentioned length correction Δ can be calculated as $\Delta = m^*/(m + aL)$ and the effective slit length is then $L_{\text{eff}} = L \cdot \Delta$. It increases with increasing mode order which is related to the SPP dispersion. Higher mode orders approach the surface plasmon energy, resulting in energies lower than expected from an ideal resonator [cf. the nonlinear relation between E and n in Fig. 3(a) for larger n]. An increasing length correction corresponds to reduced energies. In addition to the fit of the experimental data, the fit for $n = 1$ of the simulated data is also included and shows a good match with the experimental data. These findings underline the coupling behavior in double-slit systems and demonstrate that all higher harmonics are affected by the hybridization of SPP modes on the slit walls.

In addition to the energies, the wavelengths of the hybridized cavity modes were determined. Figure 4 shows the experimental SPP wavelengths λ_{exp} in a 2560-nm-long double slit in comparison to the expected nominal values of a resonator λ_{nom}, given by $2L/n$. It shows λ_{exp} at different positions along the slit close to the inner wall. The experimental wavelengths were determined by fitting a squared sine to three (two for $n = 2$) adjacent antinodes in the intensity profiles. The given error bars are composed of the sum of the standard deviation of

TABLE I. Fit parameters of the linear relationship between the reciprocal slit length $1/L$ and the energy of the hybridized cavity modes 1 to 6 and slopes m^* for corresponding electromagnetic resonators of the same length are given. The parameters a and m are only valid for experimentally relevant values of L between 0.3 and 3 μm.

N	m	a	Δ (for $L = 2$ μm)	Slope m^*
1	0.41 eV μm	0.08 eV	1.10	0.62 eV μm
1 (sim)	0.40 eV μm	0.09 eV	1.07	0.62 eV μm
2	0.80 eV μm	0.13 eV	1.16	1.24 eV μm
3	1.27 eV μm	0.14 eV	1.20	1.86 eV μm
4	1.67 eV μm	0.18 eV	1.22	2.48 eV μm
5	2.14 eV μm	0.19 eV	1.23	3.10 eV μm
6	2.56 eV μm	0.22 eV	1.24	3.72 eV μm

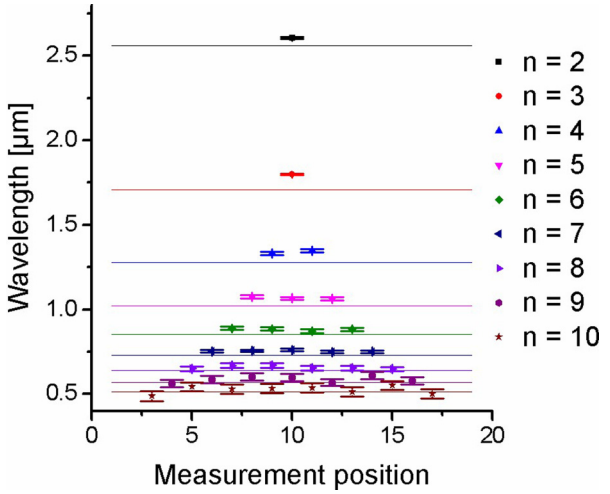

FIG. 4. Measured wavelengths in a 2560 nm slit of a double-slit system close to the inner wall. To determine the wavelengths, a square sine was fitted to three (two for $n = 2$) adjacent antinodes. The expected wavelengths are shown as horizontal lines. The errors are the sum of the standard deviation of the wavelengths for a particular n and the errors arising from the fit.

the wavelengths of a particular mode n and the error calculated by the fit. The nominal wavelengths are marked by horizontal lines. For $n = 2$ up to $n = 6$, the measured wavelengths are larger than the expected ones. The deviation from λ_{nom} decreases for increasing n. For $n \geqslant 7$, the derived wavelengths are still larger than expected, although the elongation is in the same order of magnitude as the errors. This wavelength elongation is a direct result of the energy shifts discussed in Figs. 1–3. At the inner wall, a significant redshift compared to the expected resonator energy is observed. A redshift translates into a larger wavelength, which is confirmed by the data in Fig. 4.

A complementary behavior of wavelengths was reported for Ag nanorods [38,39] and Au-Ag alloy nanowires [15], where Fabry-Perot-like SPP modes were also observed. Here, the SPP resonances are shifted by $\pi/2$ compared to the slits in accordance to Babinet's principle [40], i.e., the fundamental mode in a nanorod has two intensity maxima at the rod ends in contrast to the slit with one maximum in the center. In the metal nanorods, antinode bunching (i.e., shorter wavelengths) was observed towards rod ends, whereas the wavelength does not noticeably vary along the slit for a given mode n. Apart from that, the behavior is similar, i.e., the deviations between the nominal and experimental wavelengths are largest for the lower harmonics with λ_{exp} approaching λ_{nom} for increasing n. This complementary behavior demonstrates the correlation between slit structures and nanorods, in accordance with Babinet's principle [40].

We can now link the measured energies and wavelengths to obtain the dispersion relation of the hybridized cavity modes, as shown in Fig. 5. The dispersion of light in vacuum (light line) and the measured surface-plasmon energy of gold are also shown. Data from different slit lengths are indicated by different symbols. The wavelength of the fundamental mode was not included because it only contains a single maximum. However, profiles of the fundamental mode hint to wavelengths larger than the expected $2L$ as the intensity does not fall to zero

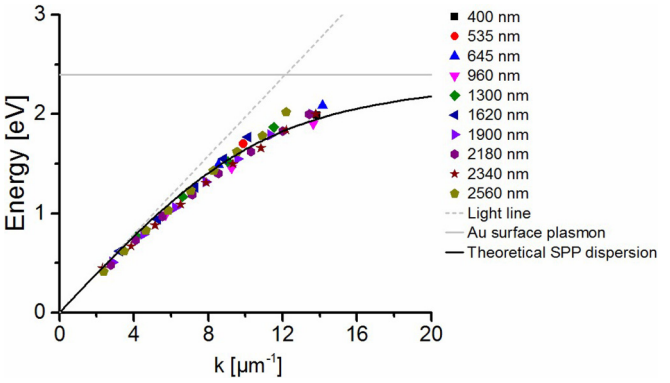

FIG. 5. Dispersion relation of the hybridized SPP cavity modes and theoretical SPP dispersion of a gold/air interface. The light line and measured energy of the Au surface plasmon are also included.

at the slit walls. For small k, the dispersion closely follows the light line. Increasing k leads to deviations from the light line, and the energy approaches the surface-plasmon energy, which is why the relation between mode order and energy in Fig. 3(a) is not linear. The theoretical SPP dispersion on the interface between gold and air, resulting from the Drude model [41], is also included in Fig. 5.

Experimental and theoretical dispersion relations agree well. At first sight, this overall good match of theoretical and experimental dispersion is unexpected. The measured SPP energies are significantly lower compared to the expected energies of a perfect electromagnetic resonator; hence, a dispersion relation with reduced energies is expected. However, the redshift of the mode energies is obviously accompanied by a corresponding wavelength elongation, leading to a negligible influence on the dispersion relation. Slightly reduced energies for wave numbers up to $9\,\mu\mathrm{m}^{-1}$ could be the result of surface contamination caused by carbon. Compared to air, this increases the local dielectric constant and lowers the surface-plasmon energy [41]. For wave numbers exceeding $9\,\mu\mathrm{m}^{-1}$, the experimental dispersion shows slightly higher energies, which is the result of the formation of symmetric and antisymmetric hybridized modes due to coupling of the two slit walls on either side of the metal bar. This structure corresponds to an insulator-metal-insulator system that is characterized by two dispersion branches due to hybridization [41]. The slightly higher energies in our data could be related to the antisymmetric hybridized mode in an insulator-metal-insulator system. However, the splitting in such a system with a large thickness of the metal film of 200 nm is only marginal. Instead, the coupling responsible for the observed deviation from the standard Au SPP dispersion takes place via the vacuum (air) space above and below the film surfaces and not through the bulk of the metal bar. The experiments of Walther *et al.* support these findings, as they have shown that the electric fields in both slits are antisymmetric for small slit distances [24,34].

III. CONCLUSIONS

The SPPs hybridized with cavity standing waves were excited by swift electrons in submicrometer double-slit systems and analyzed by high-resolution EELS in a

transmission electron microscope. Double-slit systems with lengths between 400 and 2560 nm were studied. The cavity modes are strongly amplified close to the central metal bar; a fact exploited experimentally to determine the energies, wavelengths, and detailed spatial distribution of cavity standing waves up to their 11th order. The energy of the fundamental mode could be finely tuned via the slit length to remain within a desirable energy window, between 1.0 and 0.22 eV. A significant redshift of the cavity modes in comparison to a perfect electromagnetic resonator of the same length was found close to the central metal bar in the double-slit systems correlated with the coupling with the adjacent slit. This redshift is accompanied by wavelength elongations of the cavity modes compared to the nominal ones. As a result, the measured dispersion relation of the SPP-hybridized cavity modes closely follows the dispersion expected for SPPs on a metal film. Precise knowledge of the dispersion relation, mode energies, and wavelengths is necessary to tailor SPP structures for specific applications and performance demands.

ACKNOWLEDGMENTS

This research was supported by a cooperative grant of the Karlsruhe Institute of Technology's Center for Functional Nanostructures (CFN), the Weizmann Institute Nano Initiative (WINI), and the Technion Russell Berrie Nanotechnology Institute (RBNI), and by the Weizmann's Helen and Martin Kimmel Center for Nanoscale Science (H.C.). K.B. and C.M. acknowledge support by the Deutsche Forschungsgemeinschaft (DFG) within the Priority Program SPP 1391 *Ultrafast Nanooptics* (Project Bu 1107/7-2).

[1] W. L. Barnes, A. Dereux, and T. W. Ebbesen, Surface plasmon subwavelength optics, Nature (London) **424**, 824 (2003).

[2] A. V. Zayats, I. I. Smolyaninov, and A. A. Maradudin, Nano-optics of surface plasmon polaritons, Phys. Rep. **408**, 131 (2005).

[3] K. F. MacDonald, Z. L. Samson, M. I. Stockman, and N. I. Zheludev, Ultrafast active plasmonics, Nat. Photon. **3**, 55 (2009).

[4] D. K. Gramotnev and S. I. Bozhevolnyi, Plasmonics beyond the diffraction limit, Nat. Photon. **4**, 83 (2010).

[5] P. Berini and I. De Leon, Surface plasmon-polariton amplifiers and lasers, Nat. Photon. **6**, 16 (2012).

[6] M. Schnell, A. Garcia Etxarri, A. J. Huber, K. Crozier, J. Aizpurua, and R. Hillenbrand, Controlling the near-field oscillations of loaded plasmonic nanoantennas, Nat. Photon. **3**, 287 (2009).

[7] F. J. García de Abajo, Optical excitations in electron microscopy, Rev. Mod. Phys. **82**, 209 (2010).

[8] H. Raether, Surface plasma oscillations as a tool for surface examinations, Surf. Sci. **8**, 233 (1967).

[9] J. Nelayah, M. Kociak, O. Stephan, F. J. G. de Abajo, M. Tence, L. Henrard, D. Taverna, I. Pastoriza-Santos, L. M. Liz-Marzan, and C. Colliex, Mapping surface plasmons on a single metallic nanoparticle, Nat. Phys. **3**, 348 (2007).

[10] A. S. Eggeman, P. J. Dobson, and A. K. Petford-Long, Optical spectroscopy and energy-filtered transmission electron microscopy of surface plasmons in core-shell nanoparticles, J. Appl. Phys. **101** 024307 (2007).

[11] M. Bosman, V. J. Keast, M. Watanabe, A. I. Maaroof, and M. B. Cortie, Mapping surface plasmons at the nanometre scale with an electron beam, Nanotechnology **18**, 165505 (2007).

[12] S. Aloni, Y. Yin, and A. Alivisatos, Imaging shape dependent surface plasmon modes in noble metal nanoparticles, Microsc. Microanal. **15**, 136 (2009).

[13] M. W. Chu, V. Myroshnychenko, C. H. Chen, J. P. Deng, C. Y. Mou, and F. J. G. de Abajo, Probing bright and dark surface-plasmon modes in individual and coupled noble metal nanoparticles using an electron beam, Nano Lett. **9**, 399 (2009).

[14] B. Schaffer, W. Grogger, G. Kothleitner, and F. Hofer, Comparison of EFTEM and STEM EELS plasmon imaging of gold nanoparticles in a monochromated TEM, Ultramicroscopy **110**, 1087 (2010).

[15] I. Alber, W. Sigle, S. Muller, R. Neumann, O. Picht, M. Rauber, P. A. van Aken, and M. E. Toimil-Molares, Visualization of multipolar longitudinal and transversal surface plasmon modes in nanowire dimers, ACS Nano **5**, 9845 (2011).

[16] B. S. Guiton, V. Iberi, S. Z. Li, D. N. Leonard, C. M. Parish, P. G. Kotula, M. Varela, G. C. Schatz, S. J. Pennycook, and J. P. Camden, Correlated optical measurements and plasmon mapping of silver nanorods, Nano Lett. **11**, 3482 (2011).

[17] D. Rossouw and G. A. Botton, Plasmonic Response of Bent Silver Nanowires for Nanophotonic Subwavelength Waveguiding, Phys. Rev. Lett. **110**, 066801 (2013).

[18] F. von Cube, S. Irsen, R. Diehl, J. Niegemann, K. Busch, and S. Linden, From isolated metaatoms to photonic metamaterials: Evolution of the plasmonic near-field, Nano Lett. **13**, 703 (2013).

[19] T. W. Ebbesen, H. J. Lezec, H. F. Ghaemi, T. Thio, and P. A. Wolff, Extraordinary optical transmission through sub-wavelength hole arrays, Nature (London) **391**, 667 (1998).

[20] F. J. Garcia-Vidal, L. Martin-Moreno, T. W. Ebbesen, and L. Kuipers, Light passing through subwavelength apertures, Rev. Mod. Phys. **82**, 729 (2010).

[21] W. Sigle, J. Nelayah, C. T. Koch, and P. A. van Aken, Electron energy losses in Ag nanoholes—from localized surface plasmon resonances to rings of fire, Opt. Lett. **34**, 2150 (2009).

[22] B. Ögüt, R. Vogelgesang, W. Sigle, N. Talebi, C. T. Koch, and P. A. van Aken, Hybridized metal slit eigenmodes as an illustration of Babinet's principle, ACS Nano **5**, 6701 (2011).

[23] I. Carmeli, M. A. Itskovsky, Y. Kauffmann, Y. Shaked, S. Richter, T. Maniv, and H. Cohen, Far- and near-field electron beam detection of hybrid cavity-plasmonic modes in gold microholes, Phys. Rev. B **85**, 041405 (2012).

[24] R. Walther, I. Carmeli, R. Schneider, D. Gerthsen, K. Busch, C. Matyssek, A. Shvarzman, T. Maniv, S. Richter, and H. Cohen, Interslit coupling via ultrafast dynamics across gold-film hole arrays, J. Phys. Chem. C **118**, 11043 (2014).

[25] M. Bosman and V. J. Keast, Optimizing EELS acquisition, Ultramicroscopy **108**, 837 (2008).

[26] W. H. Richardson, Bayesian-based iterative method of image restoration, J. Opt. Soc. Am. **62**, 55 (1972).

[27] L. B. Lucy, An iterative technique for the rectification of observed distributions, Astron. J. **79**, 745 (1974).

[28] J. M. Zuo, Electron detection characteristics of a slow-scan CCD camera, imaging plates and film, and electron image restoration, Microsc. Res. Tech. **49**, 245 (2000).

[29] A. Gloter, A. Douiri, M. Tence, and C. Colliex, Improving energy resolution of EELS spectra: an alternative to the monochromator solution, Ultramicroscopy **96**, 385 (2003).

[30] A. G. Al-Bakkar, S. S. Ipson, G. J. Porter, and D. G. Gleed, A parallel implementation of a modified Richardson-Lucy algorithm for image de-blurring, Int. J. Infrared Millimeter Waves **18**, 555 (1997).

[31] C. Matyssek, J. Niegemann, W. Hergert, and K. Busch, Computing electron energy loss spectra with the Discontinuous Galerkin Time-Domain method, Photon. Nanostruct. **9**, 367 (2011).

[32] K. Busch, M. Konig, and J. Niegemann, Discontinuous Galerkin methods in nanophotonics, Laser Photon. Rev. **5**, 773 (2011).

[33] P. B. Johnson and R. W. Christy, Optical constants of noble metals, Phys. Rev. B **6**, 4370 (1972).

[34] R. Walther, S. Fritz, E. Müller, R. Schneider, D. Gerthsen, W. Sigle, T. Maniv, H. Cohen, C. Matyssek, and K. Busch, Coupling of Surface-Plasmon-Polariton-Hybridized Cavity Modes between Submicron Slits in a Thin Gold Film, ACS Photon. **3**, 836 (2016).

[35] L. Novotny, Effective Wavelength Scaling for Optical Antennas, Phys. Rev. Lett. **98**, 266802 (2007).

[36] D. T. Schoen, A. C. Atre, A. García-Etxarri, J. A. Dionne, and M. L. Brongersma, Probing complex reflection coefficients in one-dimensional surface plasmon polariton waveguides and cavities using STEM EELS, Nano Lett. **15**, 120 (2015).

[37] T. Zentgraf, T. P. Meyrath, A. Seidel, S. Kaiser, H. Giessen, C. Rockstuhl, and F. Lederer, Babinet's principle for optical frequency metamaterials and nanoantennas, Phys. Rev. B **76**, 033407 (2007).

[38] D. Rossouw, M. Couillard, J. Vickery, E. Kumacheva, and G. A. Botton, Multipolar plasmonic resonances in silver nanowire antennas imaged with a subnanometer electron probe, Nano Lett. **11**, 1499 (2011).

[39] O. Nicoletti, M. Wubs, N. A. Mortensen, W. Sigle, P. A. van Aken, and P. A. Midgley, Surface plasmon modes of a single silver nanorod: An electron energy loss study, Opt. Express **19**, 15371 (2011).

[40] H. G. Booker, Slot aerials and their relation to complementary wire aerials (Babinet's principle), J. Inst. Electr. Eng. Part IIIA: Radiolocation **93**, 620 (1946).

[41] S. A. Maier, *Plasmonics: Fundamentals and Applications* (Springer Science LLC, New York, 2007).